scientific reports

Check for updates

OPEN

Ab initio structural dynamics of pure and nitrogen-containing amorphous carbon

Brad A. Steele, Sorin Bastea ✉ & I-Feng W. Kuo

Amorphous carbon (a-C) has attracted considerable interest due to its desirable properties, which are strongly dependent on its structure, density and impurities. Using ab initio molecular dynamics simulations we show that the sp^2/sp^3 content and underlying structural order of a-C produced via liquid quenching evolve at high temperatures and pressures on sub-nanosecond timescales. Graphite-like densities ($\lesssim$ 2.7 g/cc) favor the formation of layered arrangements characterized by sp^2 disordered bonding resembling recently synthesized monolayer amorphous carbon (MAC), while at diamond-like densities ($\gtrsim$ 3.3 g/cc) the resulting structures are dominated by disordered tetrahedral sp^3 hybridization typical of diamond-like amorphous carbon (DLC). At intermediate densities the system is a highly compressible mixture of coexisting sp^2 and sp^3 regions that continue to segregate over 10's of picoseconds. The addition of nitrogen (20.3%) (a-CN) generates major system features similar with those of a-C, but has the unexpected effect of reinforcing the thermodynamically disfavored carbon structural motifs at low and high densities, while inhibiting phase separation in the intermediate region. At the same time, no nitrogen elimination from the carbon framework is observed above $\simeq$ 2.8 g/cc, suggesting that nitrogen impurities are likely to remain embedded in the carbon structures during fast temperature quenches at high pressures.

The tendency of carbon to form a variety of crystalline and disordered structures is well known, and largely attributable to its ability to have three distinct hybridizations: sp^1, sp^2, and sp^3. The latter two, corresponding to 3-fold and 4-fold coordination, respectively, dominate in the solid state and characterize in turn the graphite and cubic diamond allotropes. Amorphous carbon (a-C) is a common disordered material with a complex structure determined by the relative amounts of 3-fold and 4-fold coordination present in the system[1–9], as well as density and impurities such as nitrogen (a-CN) and hydrogen (a-CH)[2,4,10–14]; the fraction of sp^3 bonding decreases for example with density[13,15–23]. Because a-C has desirable and possibly tunable mechanical, optical, and electronic properties it has been extensively studied[13,15–44] and structural defect engineering has emerged as a major avenue for designing a-C materials for specific applications[39,40]. a-C can be synthesized through a variety of ion beam and pulsed laser deposition techniques[13–17]; recently, monolayer amorphous carbon (MAC), a two-dimensional material, has been created using laser-assisted chemical vapor deposition[45]. a-C is also commonly produced during the detonation of negative oxygen balance high explosives[46–50] or through the shock-compression of organic materials via mechanisms that have not been fully elucidated yet[51,52]. Molecular dynamics (MD) simulations have been carried out to model the ion beam deposition process that is often used for a-C production, usually employing a liquid quench protocol[18–20,23,30,53–57], where liquid carbon near 5000 K is cooled to room temperature on time scales of 10's of picoseconds. Direct deposition simulations have also been performed[56,58,59] and lower quenching rates[36,60–62] have been achieved using empirical potentials and machine learning potentials such as GAP[41,58,59,61,63–65]. Whereas these efforts have been primarily aimed at better understanding the structure of a-C that is typically recovered at standard temperature and pressure conditions, the kinetic processes controlling a-C formation have been less studied. A notable exception is the work of Thapa et al.[41], which studied the formation of an amorphous graphite (a-G) material using ab initio methods up to 160 atoms and with the GAP potential up to 1000 atoms. Kinetic effects are especially important because a-C and its impurity-containing variations are metastable systems, the result of "frozen" dynamics into states whose properties are dictated by the interplay between physical and chemical processes on the one hand, and thermodynamic conditions and their rates of change on the other. It is well known for example that the phase transformation kinetics between carbon equilibrium phases has a significant pressure and temperature dependence[66–69], while the properties of precipitating carbon-rich condensed phases have a large effect on detonation events on nanosecond to microsecond

Lawrence Livermore National Laboratory, Physical and Life Sciences Directorate, 7000 East Ave., Livermore, California 94550, USA. ✉email: bastea2@llnl.gov

time-scales and are in turn strongly dependent on thermodynamic paths and associated transit times[48,49,70–78]. Herein we perform large-scale ab initio MD simulations of pure and nitrogen-containing (20.3%) liquid carbon (LC and LCN, respectively) quenches to an elevated temperature (3000 K) inside the solid region of the phase diagram, and analyze the evolution and properties of the resulting material over 10's of picoseconds time scales. The results shed new light on the formation mechanisms and characteristics of a-C and a-CN, can help guide in silico material design and synthesis efforts employing efficient atomistic methodologies[79], and may enable the development of effective models for complex phenomena such as shock-induced chemistry and detonation, which are often accompanied by the precipitation of carbon materials at high pressures and temperatures[51,52,77,78].

Results

Simulations of LC (and LCN) quenched to 3000 K were performed for densities ranging between 1.9 and 3.7 g/cc (2.0 to 3.8 g/cc, respectively). Note that LC and LCN calculations correspond to the same atomic densities. The atomic coordination vs. time for all densities are provided in the Supplementary Information (SI) Figures S2 and S3. Additional simulation details are provided in the "Methods" section.

The simulations reveal at least two distinct types of a-C structures following the temperature quench from the liquid state to the solid state region: diamond-like amorphous carbon (DLC)[2,4,10–14] and graphite-like amorphous carbon (a-G)[41]. At high densities (and pressures) the system consists mainly of 4-fold coordinated atoms with predominantly tetrahedral local structure, while the lower densities favor 3-fold coordination in a layered motif. In the intermediate regime, the (P,V) representation of the simulation results shows van der Waals loop-like behavior associated with a first order phase transformation - see Fig. 1, which is accompanied by a sharp conversion between the two dominant coordination states, sp^3 and sp^2 - see Fig. 2. Indeed, experimentally validated equations of state (EOS) for carbon[73,80] indicate that at 3000 K the diamond - graphite transformation pressure is around 10

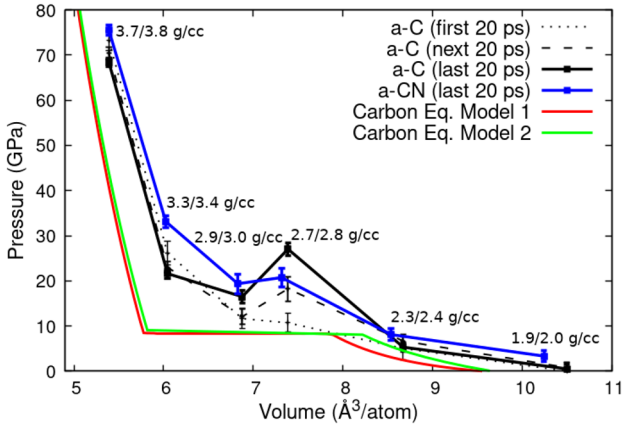

Figure 1. Pressure-volume relationship for amorphous carbon (a-C) quenched to 3000 K averaged over different time intervals. The error bars are the standard deviation with time for the given time interval. The curves are compared to carbon 3000 K isotherms calculated using two different thermodynamic models[73,80].

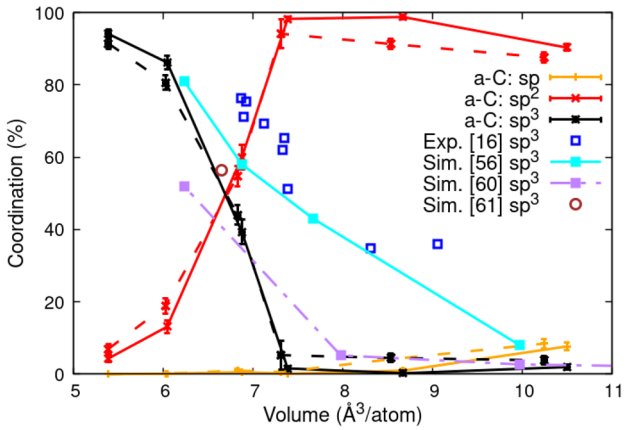

Figure 2. Atomic coordination of carbon atoms for a-C and a-CN (20.3 % N) vs. volume. The error bars are the standard deviation with time calculated for the final 20 ps of the simulations. The a-CN curves are displayed with dashed lines with the same color as a-C. The results are compared with ion deposition experiments (Exp.) by Fallon et al.[16] and simulations (Sim.) by Marks et al.[56], Ranganathan et al.[60], and Tomas et al.[61].

GPa. The simulated 3000 K isotherm is shifted to higher pressures compared with the EOS prediction, and the transition pressure (which could be estimated from the P-V curve using an approximate Maxwell construction) is accordingly larger; the volume change on the other hand is smaller than the EOS one. These differences may be due to DFT approximations and system size limitations which, while important, should not affect our analysis and conclusions. The addition of nitrogen to the system has the effect of smearing the transformation between diamond-like and graphite-like behavior by noticeably reducing the volume change between these states - see Fig. 1. This is also evident, but not as pronounced, in the coordination plot as a function of density - see Fig. 2.

At high densities, where the material is primarily sp^3 bonded, the final sp^3 fractions observed in the simulations are consistent with room temperature DFT calculations by Marks et al.[30] and ion beam deposition experiments[13,16] - see Fig. 2. At low densities on the other hand they are significantly smaller. The difference with the results by Marks et al. is probably explained by the higher temperature and longer timescales of our simulations (see also below), while the disagreement with the ion beam deposition experiments may be due to the complex heating and temperature quenching profiles likely generated by ion bombardment processes, which are not modeled in these simulations[59]. Simulations by Ranganathan et al. on timescales of 100's ps employing an empirical potential[60] agree with the current results at low densities - see Fig. 2, but underpredict the sp^3 fraction at high densities, possibly due to limitations of the empirical potential model. Liquid quench simulations by Tomas et al.[61] using a machine learning GAP potential at 3.0 g/cc and 3000 K for 200 ps appear to be consistent with the current DFT results. Tomas et al. also compare results of liquid carbon quench simulations for numerous force fields available in the literature[36,61]. However, a comparison with long-time large-scale DFT simulations, as shown here, is lacking.

Snapshots of the final simulation configurations - see Fig. 3 and SI Figure S4, show the distinct structural properties of the system at the different densities studied. In particular, the presence of layered structures is visually striking for both the a-C and a-CN simulations up to 2.9 g/cc and 3.0 g/cc, respectively, although there are also obvious differences between the systems in this region. At densities of 2.3 and 2.7 g/cc the a-C simulations exhibit uniform layering characteristic of graphite, but at 2.9 g/cc extended non-layered high density regions are also present, while the 1.9 g/cc structure appears only marginally layered with large voids. The corresponding a-CN structures are reminiscent of the a-C ones, but the 2.4 g/cc structure displays non-negligible interlayer connectivity compared with its a-C counterpart and 2.0 g/cc shows no layering at all. At the same time, nitrogen appears to be well embedded in the carbon structures, with some free molecular nitrogen only observed at the lowest densities (2.0 and 2.4 g/cc), as evidenced by the nitrogen-nitrogen radial distribution functions (RDF) (SI Figure S5) with the characteristic N_2 molecular bond peak at $\simeq$1.1Å. Interestingly, at 2.8 g/cc and 3.8 g/cc the nitrogen-nitrogen RDF exhibits a peak at $\simeq$1.34 Å, which is also present but weaker at other densities. It is worth noting that this distance is between that of a single and double nitrogen-nitrogen bond (1.45 Å in hydrazine and 1.25 Å in trans-diimine) and close to the DFT-calculated bond lengths of aromatic all-nitrogen rings (1.30 – 1.36 Å), predicted to be stable at high pressures (>15 GPa)[81–83]. We note that nitrogen-nitrogen bonds undermine the stability of N-doped graphene and other carbon-nitrogen structures[84,85].

A major feature of the present simulations is that they exhibit clear time evolution of the system bonding and structural properties over 10's of ps. This is evident for example in snapshots of the a-C (and a-CN) simulations at 2.7 g/cc (2.8 g/cc, respectively) - Figs. 4 and 5, as well as for those at 2.9 g/cc (3.0 g/cc, respectively) - SI Figures S6 and S7. However, the nature of the kinetics appears to be different at the low (and high) densities compared with the intermediate density region. To better understand the features of the unfolding kinetics we analyzed the fractions of 3-fold and 4-fold coordinated carbon atoms as a function of time, and calculated average local order parameters characterizing tetrahedral (q_{tet}) and planar hexagonal (q_{hex}) arrangements associated with these bonding states, respectively[86]. Order parameter values between 0.3 and 1 indicate structural order, with 1 corresponding to the ideal structures. The results are plotted in Fig. 6 for the a-C system at 2.7, 2.9, and 3.3 g/cc, and a-CN at 2.8, 3.0, and 3.4 g/cc.

At 2.7 g/cc the a-C fraction of 3-fold coordinated carbons increases rapidly following the temperature quench to encompass essentially the full system in approximately 60 ps, and the number of 4-fold coordinated atoms correspondingly decreases to almost zero. At the same time, the structural order parameter q_{hex} describing planar sp^2 arrangements steadily rises, while q_{tet} signals only marginal then complete loss of tetrahedral order. This is confirmed by the system snapshots - see Fig. 4, which show well defined 4-fold coordinated domains shrinking as the background layered graphitic order becomes more pronounced. Analysis of the late times structure shows regular layering - see Fig. 7a and yields an interlayer distance for the resulting material of 2.88 Å; this is identical with the value for graphite at this density and 300 K[87]. Thus, at the current conditions intralayer bonding defects are the dominant system structural disorder feature, as already suggested by q_{hex}, albeit layer corrugation is also noticeable. A close look at a single layer - see Fig. 8a, reveals a disordered lattice consisting of distorted 5, 6, 7, and 8-member rings. Although the system size is too small for detailed comparisons, the structure appears similar with that of recently synthesized monolayer amorphous carbon (MAC)[45]. At the same time, the layer thickness and interlayer distance are approximately half that of the MAC and multilayer MAC, respectively; we attribute this to the high bulk density of the current material. It may be interesting to see if a single suspended layer experiences buckling and a corresponding increase of its height profile once it is exfoliated from the present system; this will require larger scale simulations. We note that in this density range the present results are in close agreement with the ab initio simulations of Thapa et al.[41].

No nucleation effects are obvious in the simulations, with domains of identifiable phases emerging almost spontaneously (in less than 10 ps) following the quench. The subsequent ordering seems to consist of two distinct stages: in the first one the diminishing 4-fold regions are larger than the graphitic interlayer distance, while in the second one the remaining 4-fold coordinated carbons serve as independent tetrahedral interlayer bridges that gradually vanish. We speculate that at these thermodynamic conditions, which should be close to the edge of graphite - diamond coexistence, the first stage of the interphase boundary motion is driven by its

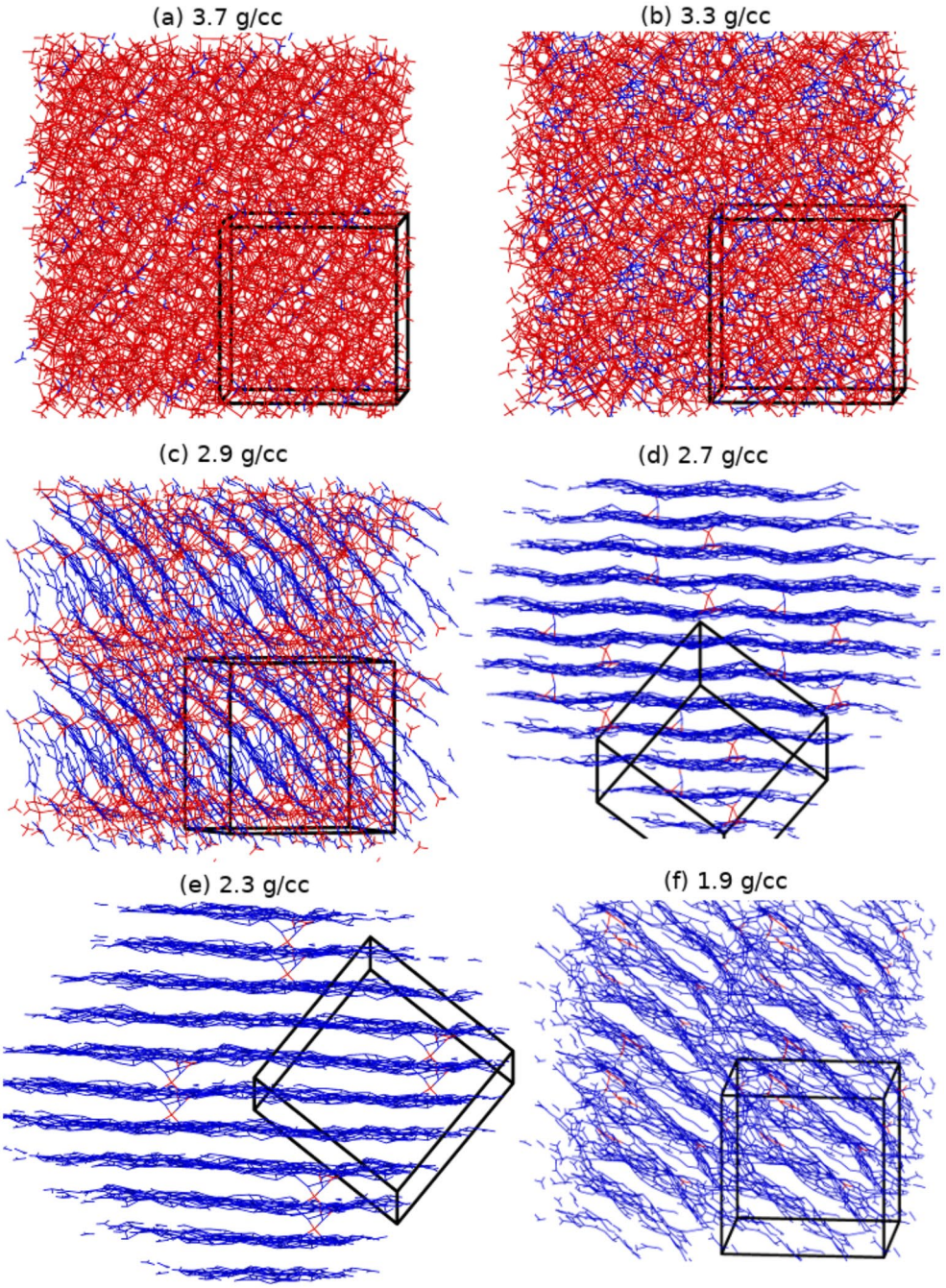

Figure 3. Snapshots of the final structure of a-C at 3000 K at each density studied. Atoms are color-coded based on the atomic coordination; 3-fold coordinated atoms are blue and 4-fold coordinated atoms are red. For visualization purposes, each image is a 2×2×2 supercell of the actual simulation cell (black box).

curvature, as in classical ordering with a non-conserved order parameter[88]. While the system size is too small to fully resolve this issue, the early time evolution of the number of bonds between 3-fold and 4-fold atoms (N_{34}), which we employ as a proxy for the interface area, seems to be consistent with this mechanism - see SI Figure S5. Motion by curvature generates a characteristic asymptotic growth law for the size of the domains, $R \propto t^{\frac{1}{2}}$[88,89]. The current simulations show that graphitic domains of order 1 nm are reached in 10's of ps, which implies that in systems of $\simeq$10 nm the transformation should require a few nanoseconds. Although direct experimental measurements are not available, experiments characterizing the precipitation of $\simeq$10 nm liquid carbon droplets during a detonation event and their solidification into graphitic nano-onions[77] suggest that the transformation occurs on time-scales that are at least an order of magnitude smaller that those of the associated adiabatic expansion, i.e. $\lesssim$10 ns. Thus, the present results are likely consistent with experimental observations and can be used to inform larger scale simulations of this process employing well-trained empirical force-fields[51,52]. They

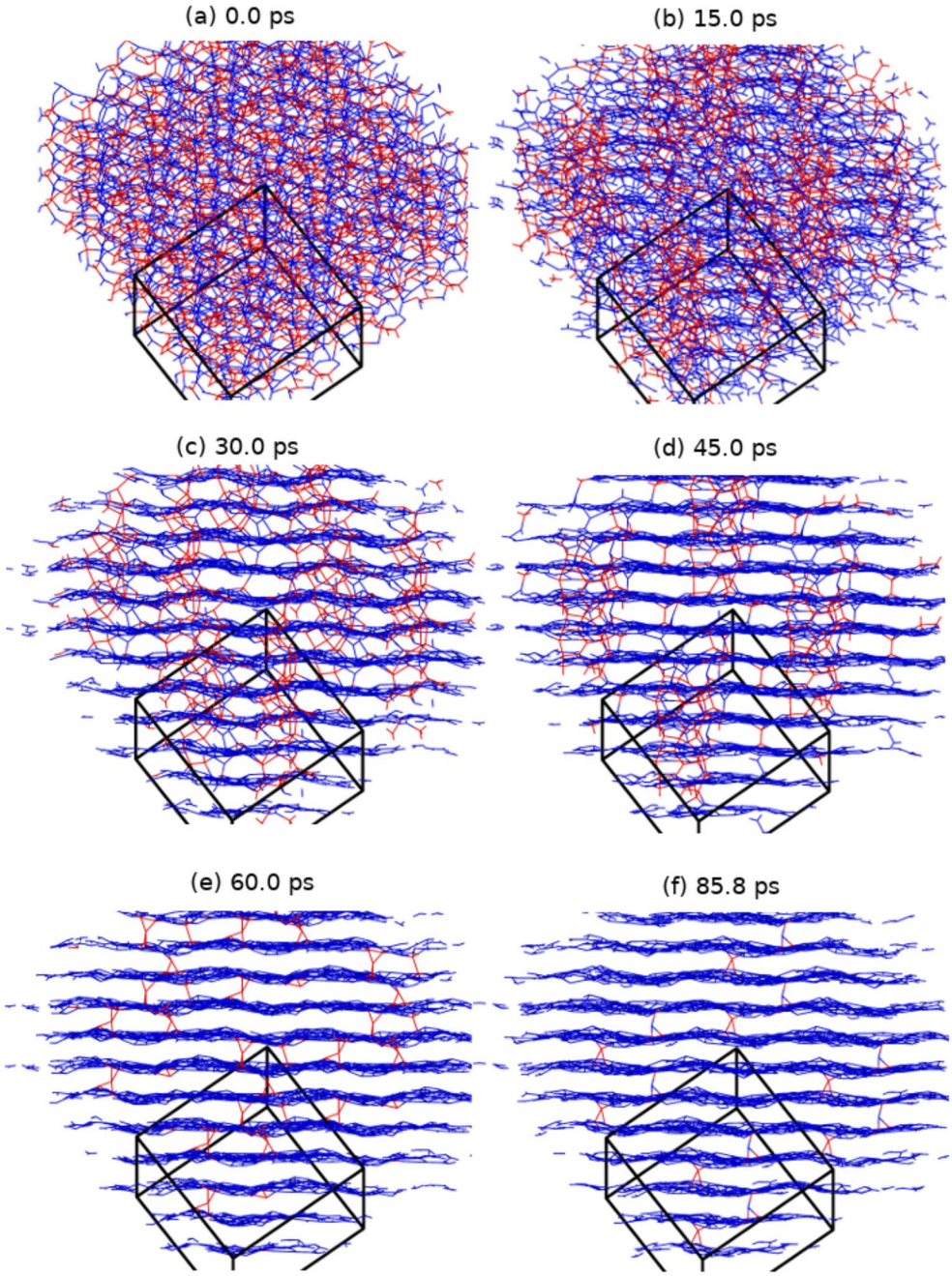

Figure 4. Structural evolution as a function of time of a-C at 3000 K and 2.7 g/cc at 0.0, 15.0, 30.0, 45.0, 60.0, and 85.8 ps showing the transformation to a layered structure. Atoms are color-coded based on the atomic coordination. For visualization purposes, each image is a 2×2×2 supercell of the actual simulation cell (black box).

are also in qualitative in agreement with detonation experiments on hydrocarbons and oxygen mixtures, which produce graphene nanosheets[90,91].

The addition of nitrogen (a-CN at 2.8 g/cc) changes subtly the carbon bonding kinetics - see Fig. 6, by slightly reducing the majority 3-fold fraction and increasing the 4-fold one. At the same time, nitrogen appears to support the tetrahedral structural order of the shrinking 4-fold coordinated phase, which persists for a long time as an interlayer reinforcement - see Fig. 5. The effect is even more pronounced at 2.4 g/cc, which displays strong interlayer connectivity compared with its 2.3 g/cc a-C counterpart. The interlayer spacing of the resulting material is approximately identical with that of a-C (at 2.7 g/cc), with most nitrogen atoms well distributed within the layers - see Fig. 7b, although the layer "thickness", as measured by the width of the particle distributions, appears to be approximately 9% larger. The single layer structure is also similar - see Fig. 8b, but the amount of intralayer bonding defects is higher for a-CN (2.8 g/cc) than a-C (2.7 g/cc), as evidenced by the larger ratio of

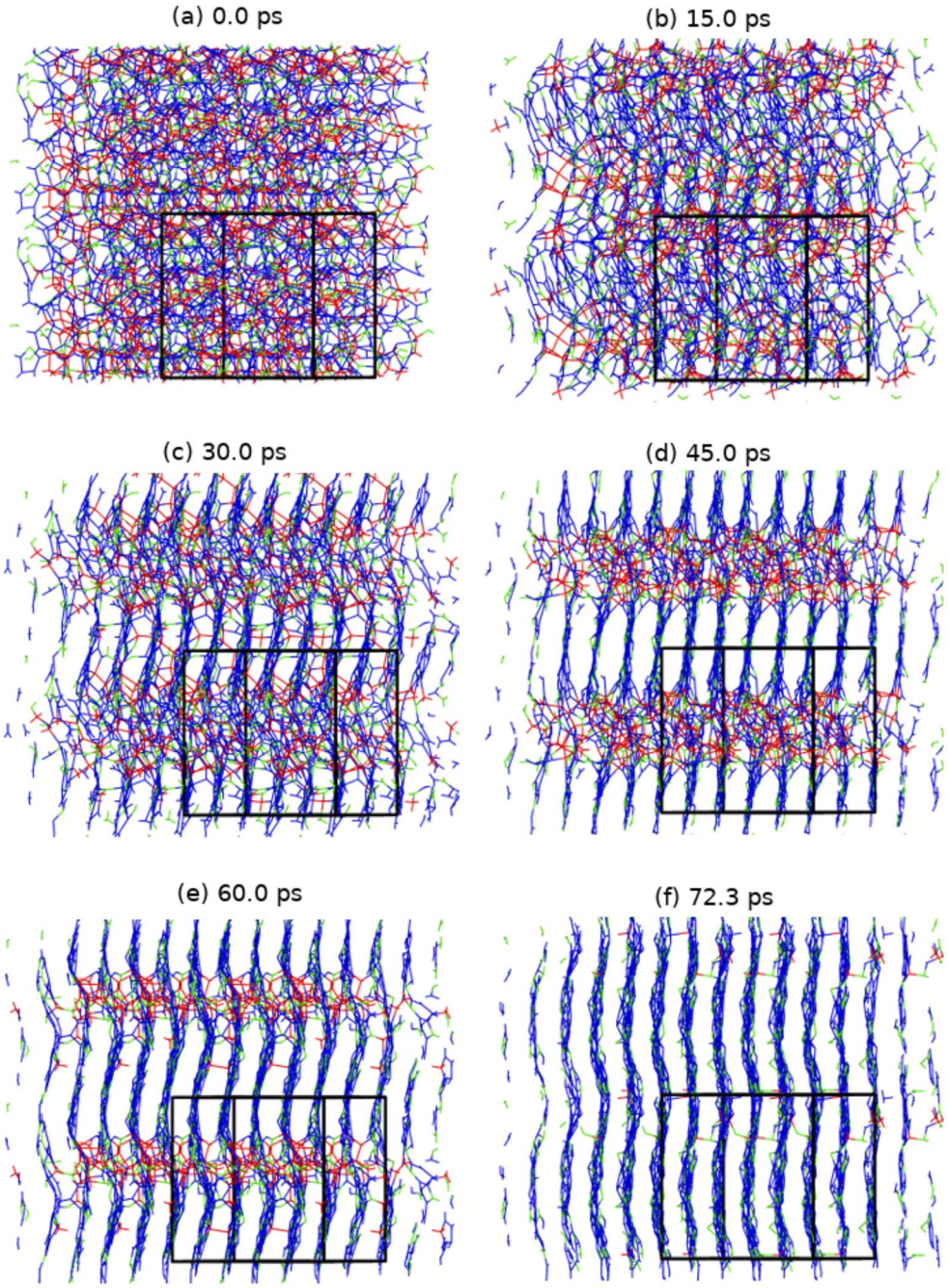

Figure 5. Structural evolution as a function of time of a-CN at 3000 K and 2.8 g/cc at 0.0, 15.0, 30.0, 45.0, 60.0, and 72.3 ps showing the transformation to a layered structure. Same coloring scheme as Fig 4 was used except for nitrogen atoms which are green. For visualization purposes, each image is a 2×2×2 supercell of the actual simulation cell (black box).

5-membered to 6-membered rings in the final structures - see SI Figure S10. This contributes to a reduction in the first peak of the carbon-carbon RDF of a-CN compared to a-C - see SI Figure S11. The enhanced intralayer bonding defects of a-CN at 2.8 g/cc are consistent with the reduction of the q_{hex} order parameter compared with a-C - see Fig. 6e. At the same time, the minority tetrahedral phase exhibits more ordering in a-CN, which also contributes to the structural differences between a-C and a-CN.

We note that layered a-CN structures have potential applications as electrocatalysts for oxygen reduction reactions because the N-doped carbons enhance electrocatalytic activity compared to platinum-loaded carbon electrodes[9,92–94]. The spin density and charge distribution near N-doped regions have been reported to be responsible for activated regions involved in catalytic reactions on N-doped graphene surfaces[95–97].

The a-C simulation at 3.3 g/cc shows that at this density the 4-fold coordinated tetrahedral order is favored over the 3-fold planar one - see Fig. 3. However, the number of 4-fold carbons seems to plateau quickly on

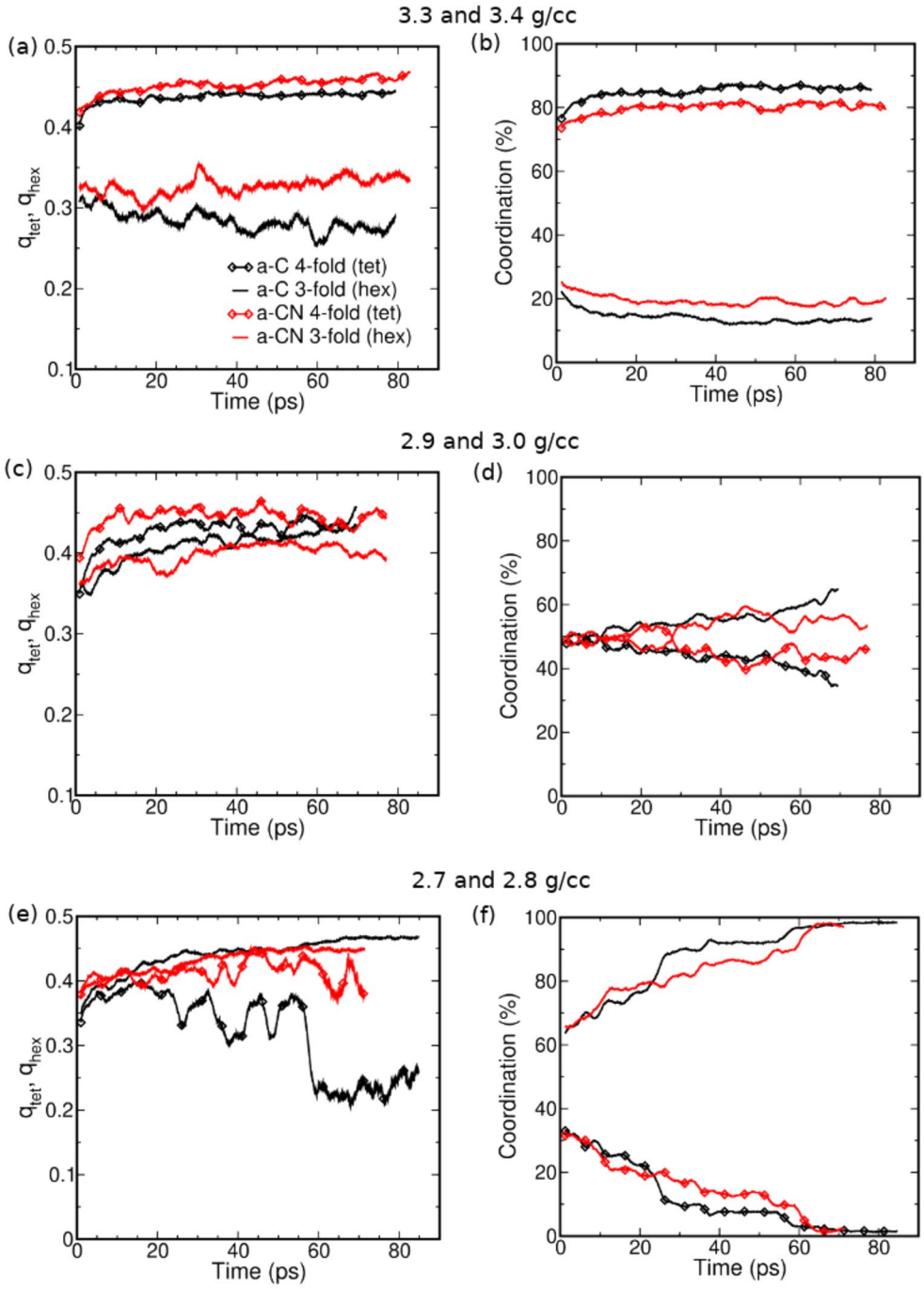

Figure 6. The tetrahedral (lines with diamond symbols) and hexagonal (lines with no symbols) order parameters (q_{tet} and q_{hex} respectively) and sp^3 and sp^2 fractions plotted as a function of time for a-C (black lines) and a-CN (red lines) at 3.3/3.4 (top), 2.9/3.0 (middle), and 2.7/2.8 g/cc (bottom) where the material is sp^3 dominant, mixed, and sp^2 dominant.

the time scales of the simulations, while at late times q_{tet} increases only very slowly, if at all. The same effect is observed at a higher density of 3.7 g/cc (not shown), where although the sp^3 fraction is slightly larger, tetrahedral ordering as quantified by q_{tet} appears to asymptote to a similar value. For both densities, small but non-negligible fractions of 3-fold carbons in locally disordered arrangements remain present for the duration of the simulations - see Fig. 6. When compared with the marked graphitic layering and the almost complete disappearance of sp^3-bonded atoms observed at 2.7 g/cc, this behavior suggests that fast temperature quenches inhibit structural ordering more efficiently at high densities (and pressures) than at lower ones. This is likely a consequence of the much slower diffusive motion occurring at these conditions - see SI Figure S6. a-CN simulations at 3.4 g/cc show evolution of the coordination fractions similar with the a-C results, but again somewhat reduced majority (4-fold) and increased minority (3-fold) populations, along with more persistent order of the minority phase,

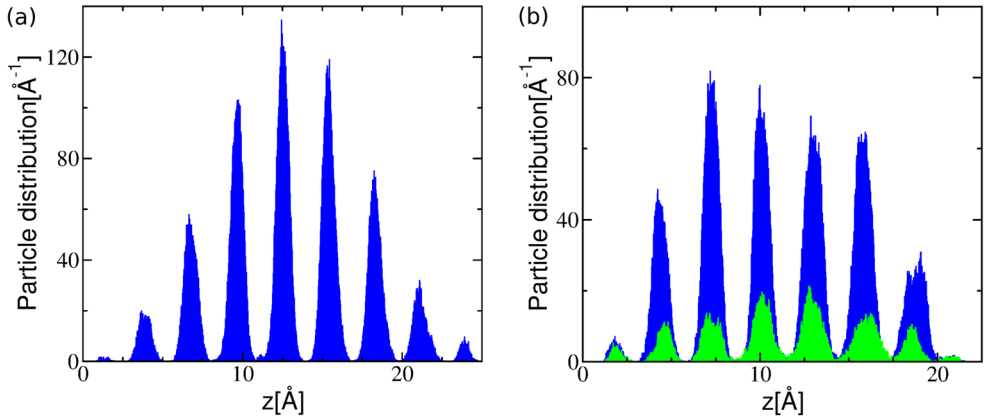

Figure 7. Particle distribution along a direction perpendicular to the layers of (**a**) a-C at 2.7 g/cc and of (**b**) a-CN at 2.8 g/cc (carbon atoms - blue, nitrogen atoms - green). Average interlayer distance is 2.88 Å.

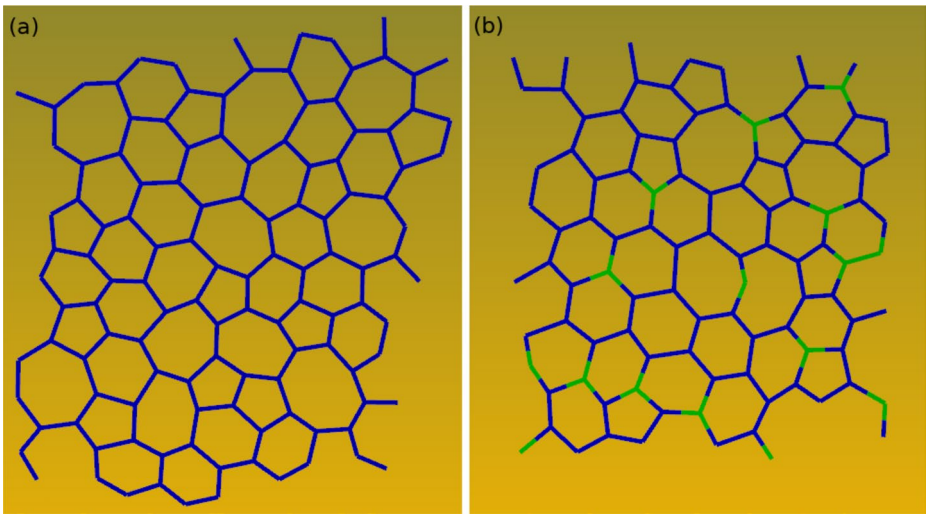

Figure 8. Bonding structure of a single layer for (**a**) a-C at 2.7 g/cc and for (**b**) a-CN at 2.8 g/cc.

as evidenced by q_{hex} - see Fig. 6. The latter effect is comparable with the one observed at 2.8 g/cc, although the minority and majority coordinations are reversed here.

The intermediate density (2.9 g/cc) a-C simulations display distinguishing characteristics compared with the ones at lower and higher densities, as can be observed in SI Figure S6. Regions of sp^3 and sp^2 coordination, the latter showing significant layering, develop during the simulation, but their relative spatial extent seems to remain almost constant. This is confirmed by the coordination fractions, which change slowly over the course of the simulations - see Fig. 6. Moreover, in contrast with the low and high density cases, the order parameters q_{tet} and q_{hex} both increase with time, indicating continuing structural ordering of the sp^3 and sp^2 regions. To better understand the nature of this process we calculated the (scaled) number of bonds between sp^3 and sp^2 carbons, $x_{34} = N_{34}/(N_3N_4)$ (here N_4 and N_3 are the number of sp^3 and sp^2 atoms, respectively); this is plotted in Fig. 9. The result shows that x_{34} decreases in time, suggesting that the sp^3 and sp^2 domains are separating and growing in time, although larger scale simulations are necessary to fully elucidate the kinetics. The corresponding a-CN system at 3.0 g/cc is visually somewhat more disordered than the a-C system - see SI Figure S7, although both the coordination fractions and order parameters display similar behavior. This is supported by the evolution of x_{34}, which remains largely constant rather than decrease in time - see Fig. 6. Thus, nitrogen appears to inhibit the growth of diamond-like and graphite-like domains, thereby promoting amorphous character. This observation is supported by the evolution of the sp^2 coordination - Fig. 6d, which increases for a-C but not a-CN, and is also consistent with the previously noted (see Fig. 1) apparent reduction of the volume change between the low and high pressure phases. To further quantify the role of nitrogen in determining the kinetic evolution of the a-CN systems we calculated the number of nitrogen - carbon bonds for all densities studied, see SI Figure S12. These are essentially time-independent, implying that carbon-bonded nitrogen remains trapped in the carbon structures over time-scales of order 100's of picoseconds and likely longer. The effect may be observable during fast temperature quenches, such as those associated with detonation events, $\gtrsim 10^9$ K/s[77].

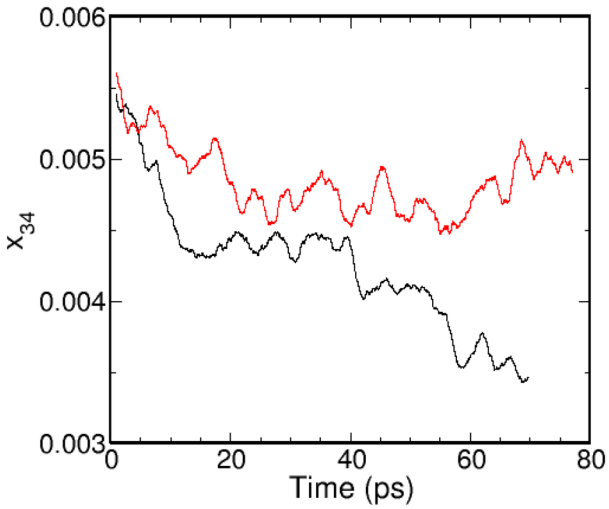

Figure 9. The change in the scaled number of bonds between 3-fold (sp^2) and 4-fold (sp^3) carbon atoms as a function of time at 2.9 g/cc for a-C (black lines) and 3.0 g/cc a-CN (red lines).

Methods

Ab initio MD simulations were performed with the Vienna Ab initio Simulation Package (VASP)[98–100]. The Perdew-Burke-Ernzerhof (PBE)[101] exchange-correlation functional under the generalized gradient approximation (GGA) was used along with projector-augmented wave (PAW) pseudo-potentials[102,103]. To account for the van der Waals forces, the Grimme semi-empirical dispersion correction[104] was also employed. A plane wave basis set with an energy cutoff of 450 eV was used along with a k-point spacing of 0.07 $Å^{-1}$. This means that the 512 atom simulations were at the Γ point in reciprocal space.

Constant temperature and volume (NVT) simulations were performed using the Nosé-Hoover thermostat with a characteristic mass corresponding to a 20 fs relaxation time[105,106]. The timestep was set to 0.5 fs and the self consistent field (SCF) convergence threshold was set to 10^{-7} eV. A Fermi smearing of electronic states was used with a width equal to $k_B T$, where k_B is the Boltzmann constant. These settings were chosen so the simulations would be conservative at the highest temperature that we considered, 9000 K.

The starting structure for the simulations was liquid carbon (LC) taken from a previous study that used 64 atoms[107,108]. LC at densities between 1.9 and 3.7 g/cc was thermalized at 9000 K for 10 ps. The temperature was then instantly reduced to 6000 K and the system was thermalized for another 10 ps. We note that at these elevated temperatures LC reaches equilibrium very rapidly. The pressure-volume curves for LC and LCN at 6000 K and 9000 K were smooth for the full pressure range, see SI Figure S1. The 64 atoms structure was then enlarged to 512 atoms to decrease finite size effects and the temperature was instantly reduced to 3000 K. Simulations at this temperature were performed for > 65 ps for each density except 1.9 g/cc, which was ran for 46 ps. Simulations with nitrogen content (thereafter denoted by LCN) were performed by randomly replacing 13 carbon atoms (or 20.3%) of the original 64 atoms LC structure with nitrogen atoms and repeating the same procedure described above starting with thermalization at 9000 K. The choice for the nitrogen concentration was loosely based on previously reported results for C-N systems as well as the properties of carbon materials recovered from detonation events[50].

Conclusions

In summary, we performed ab initio MD simulations of pure (a-C) and nitrogen-containing (20.3% N) (a-CN) amorphous carbon formation at high pressures and temperatures following a rapid quench from a liquid state to a solid state region. The results show that the system properties are determined by the competition between sp^2 and sp^3 bonding, which unfolds over 10's of picoseconds time scales and is therefore important even for very high quenching rates. We find that sp^2 and sp^3 hybridizations dominate at low and high densities, respectively, and are associated with distinct structural characteristics typical of layered (graphite-like) and tetrahedral (diamond-like) order. The layered graphite-like material is similar with the one studied by Thapa et al.[41], which the authors call amorphous graphite (a-G), while the tetrahedral one can be identified as diamond-like amorphous carbon (DLC). a-G exhibits the regular layering of graphite, but with significant intralayer disorder characterized by the presence of deformed 5, 6, 7, and 8-member rings, resembling monolayer amorphous carbon (MAC)[45]. At intermediate densities the sp^2 and sp^3-bonded carbon atoms coexist in recognizable graphitic and diamond-like domains that appear to grow in time for the pure carbon system, while the growth is kinetically inhibited when nitrogen is present. In this region the system, which we dub structurally-mixed amorphous carbon (SMAC), exhibits high compressibility inherited from the underlying diamond - graphite phase coexistence, which will affect its response to applied pressures even on sub-nanosecond time scales. The simulations indicate that the transformation from the liquid state to a graphitic solid state can proceed to completion for nanometer size systems in a fraction of a nanosecond, possibly via a mechanism controlled by interphase curvature. This is

consistent with available experimental results that detect the solidification of ≃10nm liquid carbon nano-droplets produced by detonation events into graphitic nano-onions over much shorter time scales, ≲10 ns, than those of the associated adiabatic expansion. The addition of nitrogen to the system has the surprising effect of supporting rather than disrupting the two dominant carbon structural motifs, tetrahedral and layered, even for the fairly high nitrogen concentration studied here, 20.3%. This is particularly striking for the minority phases, leading for example at lower densities to the formation of graphitic structures with persistent tetrahedral interlayer reinforcement. The resulting material has similar features with a-G, with nitrogen well intercalated in the disordered layers. No elimination of carbon-bonded nitrogen appears to occur at high densities during simulations running close to 100 ps, suggesting that at high pressures nitrogen is likely to remain embedded in the carbon structure during fast temperature quenches. The present results provide direct information on the structure and dynamics of amorphous carbon (a-C and a-CN), can serve as reference points for the generation of effective force fields capable of in silico carbon materials engineering and evaluation, and may be useful for the development of effective equations of state and kinetic models for high temperature and pressure phenomena, such as ion beam deposition, laser ablation, high pressure synthesis, shock-induced chemistry, and detonation.

Data availability

The datasets generated and/or analysed during the current study will be made available in the repository at https://nomad-lab.eu/.

Received: 28 August 2023; Accepted: 3 November 2023
Published online: 11 November 2023

References

1. Veerasamy, V. S. *et al.* Nitrogen doping of highly tetrahedral amorphous carbon. *Phys. Rev. B* **48**, 17954–17959. https://doi.org/10.1103/PhysRevB.48.17954 (1993).
2. Robertson, J. & Davis, C. A. Nitrogen doping of tetrahedral amorphous carbon. *Diam. Relat. Mater.* **4**(4), 441–444. https://doi.org/10.1016/0925-9635(94)05265-4 (1995).
3. Muhl, S. & Méndez, J. M. A review of the preparation of carbon nitride films. *Diam. Relat. Mater.* **8**(10), 1809–1830. https://doi.org/10.1016/S0925-9635(99)00142-9 (1999).
4. Kleinsorge, B., Ferrari, A. C., Robertson, J. & Milne, W. I. Influence of nitrogen and temperature on the deposition of tetrahedrally bonded amorphous carbon. *J. Appl. Phys.* **88**(2), 1149–1157. https://doi.org/10.1063/1.373790 (2000).
5. Merchant, A. & McCulloch, D. Ab initio simulations of amorphous carbon nitrides. *Phys. Rev. B* **65**(2), 024208. https://doi.org/10.1103/PhysRevB.65.024208 (2001).
6. Houska, J., Bilek, M., Warschkow, O., McKenzie, D. & Vlcek, J. Ab initio simulations of nitrogen evolution in quenched c n x and sibcn amorphous materials. *Phys. Rev. B* **72**(5), 054204. https://doi.org/10.1103/PhysRevB.72.054204 (2005).
7. Valladares, A. A. & Álvarez-Ramírez, F. Bonding in amorphous carbon-nitrogen alloys: A first principles study. *Phys. Rev. B* **73**, 024206. https://doi.org/10.1103/PhysRevB.73.024206 (2006).
8. Zheng, B. *et al.* First-principle study of nitrogen incorporation in amorphous carbon. *Carbon* **44**(5), 962–968. https://doi.org/10.1016/j.carbon.2005.10.009 (2006).
9. Zahoor, A. *et al.* Improved electrocatalytic activity of carbon materials by nitrogen doping. *Appl. Catal. B Environ.* **147**, 633–641. https://doi.org/10.1016/j.apcatb.2013.09.043 (2014).
10. Robertson, J. Hard amorphous (diamond-like) carbons. *Progr. Solid State Chem.* **21**(4), 199–333. https://doi.org/10.1016/0079-6786(91)90002-H (1991).
11. Robertson, J. Properties of diamond-like carbon. *Surf. Coat. Technol.* **50**(3), 185–203. https://doi.org/10.1016/0257-8972(92)90001-Q (1992).
12. Lifshitz, Y. Hydrogen-free amorphous carbon films: correlation between growth conditions and properties. *Diam. Relat. Mater.* **5**(3), 388–400. https://doi.org/10.1016/0925-9635(95)00445-9 (1996).
13. Ferrari, A. C. *et al.* Density, sp^3 fraction, and cross-sectional structure of amorphous carbon films determined by x-ray reflectivity and electron energy-loss spectroscopy. *Phys. Rev. B* **62**, 11089–11103. https://doi.org/10.1103/PhysRevB.62.11089 (2000).
14. Robertson, J. Diamond-like amorphous carbon. *Mater. Sci. Eng. R Rep.* **37**(4–6), 129–281 (2002).
15. McKenzie, D. R., Muller, D. & Pailthorpe, B. A. Compressive-stress-induced formation of thin-film tetrahedral amorphous carbon. *Phys. Rev. Lett.* **67**, 773–776. https://doi.org/10.1103/PhysRevLett.67.773 (1991).
16. Fallon, P. J. *et al.* Properties of filtered-ion-beam-deposited diamondlike carbon as a function of ion energy. *Phys. Rev. B* **48**, 4777–4782. https://doi.org/10.1103/PhysRevB.48.4777 (1993).
17. Chhowalla, M. *et al.* Influence of ion energy and substrate temperature on the optical and electronic properties of tetrahedral amorphous carbon (ta-c) films. *J. Appl. Phys.* **81**(1), 139–145. https://doi.org/10.1063/1.364000 (1997).
18. Wang, C. Z. & Ho, K. M. Structure, dynamics, and electronic properties of diamondlike amorphous carbon. *Phys. Rev. Lett.* **71**, 1184–1187. https://doi.org/10.1103/PhysRevLett.71.1184 (1993).
19. Mathioudakis, C., Kopidakis, G., Kelires, P. C., Wang, C. Z. & Ho, K. M. Physical trends in amorphous carbon: A tight-binding molecular-dynamics study. *Phys. Rev. B* **70**, 125202. https://doi.org/10.1103/PhysRevB.70.125202 (2004).
20. Stuart, S. J., Knippenberg, M. T., Kum, O. & Krstic, P. S. Simulation of amorphous carbon with a bond-order potential. *Phys. Scr.* **T124**, 58–64. https://doi.org/10.1088/0031-8949/2006/t124/012 (2006).
21. Han, J., Gao, W., Zhu, J., Meng, S. & Zheng, W. Density-functional theory study of the microstructure, electronic structure, and optical properties of amorphous carbon. *Phys. Rev. B* **75**, 155418. https://doi.org/10.1103/PhysRevB.75.155418 (2007).
22. Li, L. *et al.* The effect of empirical potential functions on modeling of amorphous carbon using molecular dynamics method. *Appl. Surf. Sci.* **286**, 287–297. https://doi.org/10.1016/j.apsusc.2013.09.073 (2013).
23. Bhattarai, B., Pandey, A. & Drabold, D. A. Evolution of amorphous carbon across densities: An inferential study. *Carbon* **131**, 168–174. https://doi.org/10.1016/j.carbon.2018.01.103 (2018).
24. Gilkes, K. W. R., Gaskell, P. H. & Robertson, J. Comparison of neutron-scattering data for tetrahedral amorphous carbon with structural models. *Phys. Rev. B* **51**, 12303–12312. https://doi.org/10.1103/PhysRevB.51.12303 (1995).
25. Merkulov, V. I., Lowndes, D. H., Jellison, G. E., Puretzky, A. A. & Geohegan, D. B. Structure and optical properties of amorphous diamond films prepared by arf laser ablation as a function of carbon ion kinetic energy. *Appl. Phys. Lett.* **73**(18), 2591–2593. https://doi.org/10.1063/1.122515 (1998).
26. Haerle, R., Riedo, E., Pasquarello, A. & Baldereschi, A. sp^2/sp^3 hybridization ratio in amorphous carbon from c 1*s* core-level shifts: X-ray photoelectron spectroscopy and first-principles calculation. *Phys. Rev. B* **65**, 045101. https://doi.org/10.1103/PhysRevB.65.045101 (2001).

27. Basharin, A. Y., Dozhdikov, V. S., Kirillin, A. V., Turchaninov, M. A. & Fokin, L. R. Phase diagram with a region of liquid carbon-diamond metastable states. *Tech. Phys. Lett.* **36**(6), 559–562. https://doi.org/10.1134/S1063785010060210 (2010).
28. Li, Y., Inam, F., Kumar, A., Thorpe, M. & Drabold, D. Pentagonal puckering in a sheet of amorphous graphene. *Phys. Status Solidi B* **248**(9), 2082–2086 (2011).
29. Basharin, A. Y., Lysenko, I. Y. & Turchaninov, M. A. Carbon alloy formation during graphite pulse laser melting in a medium with pressure of ≈ 10 mpa. *High Temp.* **50**(4), 464–470. https://doi.org/10.1134/S0018151X12040037 (2012).
30. Marks, N. A., McKenzie, D. R., Pailthorpe, B. A., Bernasconi, M. & Parrinello, M. Microscopic structure of tetrahedral amorphous carbon. *Phys. Rev. Lett.* **76**, 768–771. https://doi.org/10.1103/PhysRevLett.76.768 (1996).
31. Zhang, Q. *et al.* The structure and sliding friction of diamond-like carbon surfaces from molecular dynamics simulations. *Int. Jt. Tribol. Conf.* **42592**, 1043–1052 (2006).
32. Shi, Y. A mimetic porous carbon model by quench molecular dynamics simulation. *J. Chem. Phys.* **128**(23), 234707. https://doi.org/10.1063/1.2943645 (2008).
33. Tritsaris, G. A., Mathioudakis, C., Kelires, P. C. & Kaxiras, E. Optical and elastic properties of diamond-like carbon with metallic inclusions: A theoretical study. *J. Appl. Phys.* **112**(10), 103503. https://doi.org/10.1063/1.4765721 (2012).
34. Li, Y. & Drabold, D. Symmetry breaking and low energy conformational fluctuations in amorphous graphene. *Phys. Status Solidi B* **250**(5), 1012–1019 (2013).
35. Dozhdikov, V. S., Basharin, A. Y. & Levashov, P. R. Quenching of liquid carbon under intensive heat transfer to the cold diamond substrate: Molecular-dynamic simulation. *J. Phys. Conf. Ser.* **653**, 012091. https://doi.org/10.1088/1742-6596/653/1/012091 (2015).
36. de Tomas, C., Suarez-Martinez, I. & Marks, N. A. Graphitization of amorphous carbons: A comparative study of interatomic potentials. *Carbon* **109**, 681–693. https://doi.org/10.1016/j.carbon.2016.08.024 (2016).
37. Bhattarai, B. & Drabold, D. A. Amorphous carbon at low densities: An ab initio study. *Carbon* **115**, 532–538. https://doi.org/10.1016/j.carbon.2017.01.031 (2017).
38. Bhattarai, B., Biswas, P., Atta-Fynn, R. & Drabold, D. A. Amorphous graphene: a constituent part of low density amorphous carbon. *Phys. Chem. Chem. Phys.* **20**(29), 19546–19551. https://doi.org/10.1039/C8CP02545B (2018).
39. Tian, W. *et al.* Porous carbons: Structure-oriented design and versatile applications. *Adv. Funct. Mater.* **30**, 1909265. https://doi.org/10.1002/adfm.201909265 (2020).
40. Zhu, J. & Mu, S. Defect engineering in carbon-based electrocatalysts:insight into intrinsic carbon defects. *Adv. Funct. Mater.* **30**, 2001097. https://doi.org/10.1002/adfm.202001097 (2020).
41. Thapa, R., Ugwumadu, C., Nepal, K., Trembly, J. & Drabold, D. Ab initio simulation of amorphous graphite. *Phys. Rev. Lett.* **128**(23), 236402. https://doi.org/10.1103/PhysRevLett.128.236402 (2022).
42. Ugwumadu, C. *et al.* Simulation of multi-shell fullerenes using machine-learning gaussian approximation potential. *Carbon Trends* **10**, 100239. https://doi.org/10.1016/j.cartre.2022.100239 (2023).
43. Ugwumadu, C., Nepal, K. & Thapa, R. Atomistic nature of amorphous graphite. *Phys. Chem. Glas. Eur. J. Glass Sci. Technol. Part B* **64**(1), 16–22 (2023).
44. Ugwumadu, C., Thapa, R., Al-Majali, Y., Trembly, J. & Drabold, D. Formation of amorphous carbon multi-walled nanotubes from random initial configurations. *Phys. Status Solidi b* **260**(3), 2200527 (2023).
45. Toh, C.-T. *et al.* Synthesis and properties of free-standing monolayer amorphous carbon. *Nature* **577**, 199. https://doi.org/10.1038/s41586-019-1871-2 (2020).
46. Kuznetsov, A. *et al.* Effect of explosion conditions on the structure of detonation soots: Ultradisperse diamond and onion carbon. *Carbon* **32**, 873–882. https://doi.org/10.1016/0008-6223(94)90044-2 (1994).
47. Chen, P., Huang, F. & Yun, S. Characterization of the condensed carbon in detonation soot. *Carbon* **41**(11), 2093–2099. https://doi.org/10.1016/S0008-6223(03)00229-X (2003).
48. Hammons, J. A. *et al.* Submicrosecond aggregation during detonation synthesis of nanodiamond. *J. Phys. Chem. Lett.* **12**(22), 5286–5293. https://doi.org/10.1021/acs.jpclett.1c01209 (2021).
49. Reeves, R.V., Egan, G.C., Klunder, G.L., Manaa, M.R., & Bastea, S.: An experimental characterization of condensed phase soot from overdriven detonation of composition b. *AIP Conf. Proc.* AIP Publishing LLC **1979**, 100033 (2018). https://doi.org/10.1063/1.5044905.
50. Christenson, J. *et al.* The role of detonation condensates on the performance of 1,3,5-triamino-2,4,6-trinitrobenzene (tatb) detonation. *J. Appl. Phys.* **132**, 095901. https://doi.org/10.1063/5.0091799 (2022).
51. Armstrong, M. *et al.* Ultrafast shock synthesis of nanocarbon from a liquid precursor. *Nat. Commun.* **11**, 353. https://doi.org/10.1038/s41467-019-14034-z (2020).
52. Lindsey, R., Goldman, N., Fried, L. & Bastea, S. Chemistry-mediated Ostwald ripening in carbon-rich C/O systems at extreme conditions. *Nat. Commun.* **13**, 1424. https://doi.org/10.1038/s41467-022-29024-x (2022).
53. Galli, G., Martin, R. M., Car, R. & Parrinello, M. Carbon: The nature of the liquid state. *Phys. Rev. Lett.* **63**(9), 988. https://doi.org/10.1103/PhysRevLett.63.988 (1989).
54. Galli, G., Martin, R. M., Car, R. & Parrinello, M. Melting of diamond at high pressure. *Science* **250**(4987), 1547–1549. https://doi.org/10.1126/science.250.4987.154 (1990).
55. Grumbach, M. P. & Martin, R. M. Phase diagram of carbon at high pressures and temperatures. *Phys. Rev. B* **54**, 15730–15741. https://doi.org/10.1103/PhysRevB.54.15730 (1996).
56. Marks, N. Modelling diamond-like carbon with the environment-dependent interaction potential. *J. Phys. Condens. Matter* **14**(11), 2901. https://doi.org/10.1088/0953-8984/14/11/308 (2002).
57. Caro, M. A., Zoubkoff, R., Lopez-Acevedo, O. & Laurila, T. Atomic and electronic structure of tetrahedral amorphous carbon surfaces from density functional theory: Properties and simulation strategies. *Carbon* **77**, 1168–1182. https://doi.org/10.1016/j.carbon.2014.06.060 (2014).
58. Caro, M. A., Deringer, V. L., Koskinen, J., Laurila, T. & Csányi, G. Growth mechanism and origin of high sp3 content in tetrahedral amorphous carbon. *Phys. Rev. Lett.* **120**(16), 166101. https://doi.org/10.1103/PhysRevLett.120.166101 (2018).
59. Caro, M. A., Csányi, G., Laurila, T. & Deringer, V. L. Machine learning driven simulated deposition of carbon films: From low-density to diamondlike amorphous carbon. *Phys. Rev. B* **102**(17), 174201. https://doi.org/10.1103/PhysRevB.102.174201 (2020).
60. Ranganathan, R., Rokkam, S., Desai, T. & Keblinski, P. Generation of amorphous carbon models using liquid quench method: A reactive molecular dynamics study. *Carbon* **113**, 87–99. https://doi.org/10.1016/j.carbon.2016.11.024 (2017).
61. de Tomas, C. *et al.* Transferability in interatomic potentials for carbon. *Carbon* **155**, 624–634. https://doi.org/10.1016/j.carbon.2019.07.074 (2019).
62. Qamar, M., Mrovec, M., Lysogorskiy, Y., Bochkarev, A. & Drautz, R. Atomic cluster expansion for quantum-accurate large-scale simulations of carbon. *J. Chem. Theory Comput.* **19**(15), 5151–5167. https://doi.org/10.1021/acs.jctc.2c01149 (2023).
63. Deringer, V. L. & Csányi, G. Machine learning based interatomic potential for amorphous carbon. *Phys. Rev. B* **95**(9), 094203. https://doi.org/10.1103/PhysRevB.95.094203 (2017).
64. Jana, R., Savio, D., Deringer, V. L. & Pastewka, L. Structural and elastic properties of amorphous carbon from simulated quenching at low rates. *Modell. Simul. Mater. Sci. Eng.* **27**(8), 085009 (2019).
65. Rowe, P., Deringer, V. L., Gasparotto, P., Csányi, G. & Michaelides, A. An accurate and transferable machine learning potential for carbon. *J. Chem. Phys.* **153**(3), 45696514 (2020).

66. Bundy, F. Direct conversion of graphite to diamond in static pressure apparatus. *J. Chem. Phys.* **38**(3), 631–643 (1963).
67. Bundy, F. P. *et al.* The pressure-temperature phase and transformation diagram for carbon; updated through 1994. *Carbon* **34**(2), 141–153. https://doi.org/10.1016/0008-6223(96)00170-4 (1996).
68. Xiao, P. & Henkelman, G. Communication: From graphite to diamond: Reaction pathways of the phase transition. *J. Chem. Phys.* **137**(10), 101101. https://doi.org/10.1063/1.4752249 (2012).
69. Stavrou, E. *et al.* Detonation-induced transformation of graphite to hexagonal diamond. *Phys. Rev. B* **102**, 104116. https://doi.org/10.1103/PhysRevB.102.104116 (2020).
70. Mochalin, V. N., Shenderova, O., Ho, D. & Gogotsi, Y. The properties and applications of nanodiamonds. *Nat. Nanotechnol.* **7**, 11 (2012).
71. Shaw, M. & Johnson, J. Carbon clustering in detonations. *J. Appl. Phys.* **62**(5), 2080–2085 (1987).
72. Titov, V. M., Anisichkin, V. F. & Mal'kov, I. Y. Synthesis of ultradispersed diamond in detonation waves. *Combust. Explos. Shock Waves* **25**(3), 372–379. https://doi.org/10.1007/BF00788819 (1989).
73. Viecelli, J. A., Bastea, S., Glosli, J. N. & Ree, F. H. Phase transformations of nanometer size carbon particles in shocked hydrocarbons and explosives. *J. Chem. Phys.* **115**(6), 2730–2736. https://doi.org/10.1063/1.1386418 (2001).
74. Bastea, S. Aggregation kinetics of detonation nanocarbon. *Appl. Phys. Lett.* **100**, 214106. https://doi.org/10.1063/1.4722783 (2012).
75. Dubois, V. & Pineau, N. New developments of the carte thermochemical code: A two-phase equation of state for nanocarbons. *J. Appl. Phys.* **119**(1), 015903 (2016).
76. Bastea, S. Nanocarbon condensation in detonation. *Sci. Rep.* **7**, 42151. https://doi.org/10.1038/srep42151 (2017).
77. Bagge-Hansen, M. *et al.* Detonation synthesis of carbon nano-onions via liquid carbon condensation. *Nat. Commun.* **10**, 3819. https://doi.org/10.1038/s41467-019-11666-z (2019).
78. Lindsey, R. K., Bastea, S., Goldman, N. & Fried, L. E. Investigating 3,4-bis(3-nitrofurazan-4-yl)furoxan detonation with a rapidly tuned density functional tight binding model. *J. Chem. Phys.* **154**, 164115. https://doi.org/10.1063/5.0157238 (2021).
79. Deringer, V. L. *et al.* Gaussian process regression for materials and molecules. *Chem. Rev.* **121**, 10073 (2021).
80. Fried, L. E. & Howard, W. M. Explicit gibbs free energy equation of state applied to the carbon phase diagram. *Phys. Rev. B* **61**, 8734–8743. https://doi.org/10.1103/PhysRevB.61.8734 (2000).
81. Steele, B. A. & Oleynik, I. I. Sodium pentazolate: A nitrogen rich high energy density material. *Chem. Phys. Lett.* **643**, 21–26 (2016).
82. Steele, B. A. *et al.* High-pressure synthesis of a pentazolate salt. *Chem. Mater.* **29**(2), 735–741 (2017).
83. Laniel, D. *et al.* Aromatic hexazine [n6] 4- anion featured in the complex structure of the high-pressure potassium nitrogen compound k9n56. *Nat. Chem.* **52**, 1–6 (2023).
84. Chaban, V. V. & Prezhdo, O. V. Nitrogen-nitrogen bonds undermine stability of n-doped graphene. *J. Am. Chem. Soc.* **137**(36), 11688–11694 (2015).
85. Chaban, V. V. & Prezhdo, O. V. Synergistic amination of graphene: Molecular dynamics and thermodynamics. *J. Phys. Chem. Lett.* **6**(21), 4397–4403 (2015).
86. Zimmermann, N. E., Horton, M. K., Jain, A. & Haranczyk, M. Assessing local structure motifs using order parameters for motif recognition, interstitial identification, and diffusion path characterization. *Front. Mater.* **4**, 34 (2017).
87. Hanfland, M., Beister, H. & Syassen, K. Graphite under pressure: Equation of state and first-order raman modes. *Phys. Rev. B* **39**, 12598 (1989).
88. Bray, A. Theory of phase-ordering kinetics. *Adv. Phys.* **43**, 357 (1994).
89. Allen, S. & Cahn, J. A microscopic theory for antiphase boundary motion and its application to antiphase domain coarsening. *Acta Metall.* **27**, 1085 (1979).
90. Nepal, A., Singh, G. P., Flanders, B. N. & Sorensen, C. M. One-step synthesis of graphene via catalyst-free gas-phase hydrocarbon detonation. *Nanotechnology* **24**(24), 245602 (2013).
91. Wright, J. P. *et al.* Synthesis of turbostratic nanoscale graphene via chamber detonation of oxygen/acetylene mixtures. *Nano Sel.* **3**(6), 1054–1068 (2022).
92. Gong, K., Du, F., Xia, Z., Durstock, M. & Dai, L. Nitrogen-doped carbon nanotube arrays with high electrocatalytic activity for oxygen reduction. *Science* **323**(5915), 760–764 (2009).
93. Qu, L., Liu, Y., Baek, J.-B. & Dai, L. Nitrogen-doped graphene as efficient metal-free electrocatalyst for oxygen reduction in fuel cells. *ACS Nano* **4**(3), 1321–1326 (2010).
94. Wood, K. N., O'Hayre, R. & Pylypenko, S. Recent progress on nitrogen/carbon structures designed for use in energy and sustainability applications. *Energy Environ. Sci.* **7**(4), 1212–1249 (2014).
95. Zhang, L. & Xia, Z. Mechanisms of oxygen reduction reaction on nitrogen-doped graphene for fuel cells. *J. Phys. Chem. C* **115**(22), 11170–11176 (2011).
96. Hou, M., Zhang, X., Yuan, S. & Cen, W. Double graphitic-n doping for enhanced catalytic oxidation activity of carbocatalysts. *Phys. Chem. Chem. Phys.* **21**(10), 5481–5488 (2019).
97. Dinadayalane, T., Lazare, J., Alzaaqi, N.F., Herath, D., Hill, B., & Campbell, A.E.: Chapter 9 - structures, properties, and applications of nitrogen-doped graphene. In: Dinadayalane, T., Hagelberg, F. (eds.) *Properties and Functionalization of Graphene. Theoretical and Computational Chemistry*, vol. 21, pp. 211–248. (Elsevier, Amsterdam, 2022). https://doi.org/10.1016/B978-0-12-819514-7.00010-5
98. Kresse, G. & Hafner, J. Ab initio molecular dynamics for liquid metals. *Phys. Rev. B* **47**, 558–561. https://doi.org/10.1103/PhysRevB.47.558 (1993).
99. Kresse, G. & Furthmiiller, J. Efficiency of ab-initio total energy calculations for metals and semiconductors using a plane-wave basis set. *Comp. Mat. Sci.* **6**(1), 15–50 (1996).
100. Kresse, G. & Furthmüller, J. Efficient iterative schemes for ab initio total-energy calculations using a plane-wave basis set. *Phys. Rev. B* **54**, 11169–11186. https://doi.org/10.1103/PhysRevB.54.11169 (1996).
101. Perdew, J. P., Burke, K. & Ernzerhof, M. Generalized gradient approximation made simple. *Phys. Rev. Lett.* **77**, 3865–3868. https://doi.org/10.1103/PhysRevLett.77.3865 (1996).
102. Blochl, P. E. Projector augmented-wave method. *Phys. Rev. B* **50**(24), 17953 (1994).
103. Kresse, G. & Joubert, D. From ultrasoft pseudopotentials to the projector augmented-wave method. *Phys. Rev. B* **59**(3), 1758–1775 (1999).
104. Grimme, S. Semiempirical GGA-Type Density Functional Constructed with a Long-Range Dispersion Correction. *J. Comp. Chem.* **27**(15), 1787–1799. https://doi.org/10.1002/jcc (2006).
105. Nosé, S. A unified formulation of the constant temperature molecular dynamics methods. *J. Chem. Phys.* **81**(1), 511. https://doi.org/10.1063/1.447334 (1984).
106. Hoover, W. G. Canonical dynamics: Equilibrium phase-space distributions. *Phys. Rev. A* **31**, 1695–1697. https://doi.org/10.1103/PhysRevA.31.1695 (1985).
107. Benedict, L. X. *et al.* Multiphase equation of state for carbon addressing high pressures and temperatures. *Phys. Rev. B* **89**, 224109. https://doi.org/10.1103/PhysRevB.89.224109 (2014).
108. Millot, M., Celliers, P.M., Sterne, P.A., Benedict, L.X., Correa, A.A., Hamel, S., Ali, S.J., Baker, K.L., Berzak Hopkins, L.F., Biener, J., Collins, G.W., Coppari, F., Divol, L., Fernandez-Panella, A., Fratanduono, D.E., Haan, S.W., Le Pape, S., Meezan, N.B., Moore,

A.S., Moody, J.D., Ralph, J.E., Ross, J.S., Rygg, J.R., Thomas, C., Turnbull, D.P., Wild, C., Eggert, J.H. Measuring the shock impedance mismatch between high-density carbon and deuterium at the national ignition facility. *Phys. Rev. B* **97**, 144108. https://doi.org/10.1103/PhysRevB.97.144108 (2018).

Acknowledgements
We would like to thank Rebecca Lindsey for insightful discussions and Sebastien Hamel for providing structure files used in this work. This work was performed under the auspices of the U.S. Department of Energy by Lawrence Livermore National Laboratory under Contract DE-AC52-07NA27344 and was funded by the ASC/PEM Program. LLNL M&IC computational resources are gratefully acknowledged. The manuscript has been approved for unlimited release under release number LLNL-JRNL-850105.

Author contributions
B.A.S.: Conceptualization, methodology, formal analysis, investigation, writing—review & Editing. S.B.: Conceptualization, methodology, formal analysis, investigation, writing - original draft, review & editing, supervision. I-F.W.K.: Conceptualization, methodology, investigation, writing—review & editing.

Competing Interests
The authors declare no competing interests.

Additional information
Supplementary Information The online version contains supplementary material available at https://doi.org/10.1038/s41598-023-46642-7.

Correspondence and requests for materials should be addressed to S.B.

Reprints and permissions information is available at www.nature.com/reprints.

Publisher's note Springer Nature remains neutral with regard to jurisdictional claims in published maps and institutional affiliations.